Antigen Geometry Tunes Mast Cell Signaling Through Distinct FcεRI Aggregation and Structural Changes

Derek A. Rinaldi[1#], William K. Kanagy[1,4#], Hannah C. Kaye[1], Rachel M. Grattan[1], Shayna R. Lucero[1], Marelessis Palomino Pérez[1], Michael J. Wester[2], Keith A. Lidke[2,3], Bridget S. Wilson[1,3], Diane S. Lidke*[1,3]

Affiliations:

[1]Department of Pathology, [2]Department Physics and Astronomy, and [3]Comprehensive Cancer Center, University of New Mexico, Albuquerque, NM 87131

Running Title: Antigen geometry tunes FcεRI signaling

[4]Present address: Department of Immunology, University of Minnesota, Minneapolis, MN 55455

# These authors contributed equally to this work.

*Correspondence: dlidke@salud.unm.edu

Abstract

Immunoreceptor tyrosine-based activation motif (ITAM)-containing Fc receptors are critical components of the innate and adaptive immune systems. FcεRI mediates the allergic response via crosslinking of IgE-bound receptors by multivalent antigens. Yet, the underlying molecular mechanisms that govern the response of FcεRI to specific antigens remain poorly understood. We compared responses induced by two antigens with distinct geometries, high valency DNP-BSA and trivalent DF3, and found unique secretion and receptor phosphorylation profiles that are due to differential recruitment of Lyn and SHIP1. To understand how these two antigens can cause such markedly different outcomes, we used direct stochastic optical reconstruction microscopy (dSTORM) super-resolution imaging combined with Bayesian Grouping of Localizations (BaGoL) analysis to compare the nanoscale characteristics of FcεRI aggregates. DF3 aggregates were found to be smaller and more densely packed than DNP-BSA aggregates. Using lifetime-based Förster resonance energy transfer (FRET) measurements, we discovered that FcεRI subunits undergo structural rearrangements upon crosslinking with either antigen, and in response to interaction with monovalent antigen presented on a supported lipid bilayer. The extent of conformational change is positively correlated with signaling efficiency. Finally, we provide evidence for forces in optimizing FcεRI signaling, such that immobilizing DF3 on a rigid surface promoted degranulation while increasing DNP-BSA flexibility lowered degranulation. These results provide a link between the physical attributes of allergens, including size, shape, valency, and flexibility, and FcεRI signaling strength. Thus, the antigen modulates mast cell outcomes by creating unique aggregate geometries that tune FcεRI conformation, phosphorylation and signaling partner recruitment.

Statement of Significance

This work elucidates the molecular mechanisms underlying differential FcεRI signaling responses induced by antigens of distinct geometries. By combining super-resolution imaging and biophysical techniques, we demonstrate that the physical attributes of allergens, including shape, flexibility, and valency, modulate mast cell signaling outcomes by altering FcεRI aggregate organization and conformational states. This provides novel insights into the structure-function relationships governing FcεRI signal transduction and its role in mast cell activation. Overall, this work establishes a link between allergen physical properties and immune receptor signaling at the molecular level, with important implications for understanding and regulating allergic responses.

Introduction

Mast cells respond to a variety of antigens and allergens via immunoglobulin E (IgE)-mediated FcεRI signaling. These range from antigens presented on the surface of parasites (1) to multivalent pollen grains (2), down to food-derived peptide fragments (3, 4) and toxins/venoms (5). How the properties of antigens influence the mast cell response has been a long-standing question in the field, with evidence that FcεRI signaling is sensitive to a wide variety of antigen properties including affinity, valency, epitope spacing, size and dose (6–15). Several groups have developed synthetic antigens to evaluate how manipulating physical properties changes FcεRI signaling. Baird and colleagues used DNP-conjugated DNA to generate bivalent or trivalent ligands of specific length (9–11) and determined that bivalent DNA ligands cause degranulation up to a spacing of 5.5 nm but signaling was lost at a ligand spacing of 6.8 nm (11). Increasing the valency to three with a Y-shaped DNA structure resulted in degranulation up to 10.4 nm spacing (10). Posner et al compared flexible PEG-based bivalent and trivalent ligands with spacing ~4-5 nm and found that trivalent ligands cause more efficient mast cell secretion, with longer linkers providing increased response, and bivalent ligands were unable to cause activation at any dose (16). Mahajan et al constructed a well-defined trivalent DNP antigen out of the symmetrically arrayed T4 fibritin foldon domain (~ 3.4 nm spacing between DNP haptens), termed DF3, and found dose dependent increases in secretion up to a 300 nM threshold, above which degranulation was reduced in both RBL cells and bone marrow mast cells (BMMCs). This effect, called high-dose inhibition, was linked to changes in receptor aggregate size and ITAM phosphorylation (6). Moving towards the study of natural allergens, Gieras et al introduced the grass pollen allergen epitope, Phl P 1, on either the N- or C-terminus of myoglobin, ranging in valency from 1-4 (8, 17). They found that the higher valency MB4N (4 epitopes together on N-terminus) caused more severe anaphylaxis responses *in vivo* than the bivalent variants. Using negative stain electron microscopy (EM), they showed that the variety of IgE immune complexes increased with epitope valency and proximity. Wilson and colleagues took a reverse approach to investigate the requirements of the highly potent shrimp tropomyosin allergen, Pen a 1, by comparing the full allergen to pepsin-digested fragments. They found that immunogenicity was retained after intermediate digestion, with small fragments of 60-79 amino acids capable of weak signaling, and losses in mast cell response only noted after prolonged digestion (7). While multivalency is a well-accepted requirement for receptor activation, we and others have shown that monovalent ligand can support mast cell secretion and cytokine production when presented in a fluid supported lipid bilayer (SLB) (13–15), suggesting that the application of force may also play a role in FcεRI activation. These studies show that allergens can tune the mast cell response based on their physical properties, but the question remains: What are the underlying molecular mechanisms that govern the differential response of FcεRI to specific antigens?

FcεRI is a heterotetrametric complex consisting of an α-subunit, a β-subunit and two disulfide-linked γ-subunits. The α-subunit binds circulating IgE with nanomolar affinity (18). Crosslinking of IgE-bound receptor by multivalent antigen leads to recruitment of the Src Family Kinase (SFK) Lyn that phosphorylates ITAMs (immunoreceptor tyrosine-based activation motifs) on the β and γ_2 subunits. Signaling is then propagated by recruitment of SH2-containing downstream signaling molecules to phosphorylated ITAMs (19–22). The β-subunit is typically considered a

negative regulator through SH2-mediated recruitment of phosphatases, such as SHIP1 (6, 23–25), while the γ_2 subunits primarily drive positive signaling through recruitment of Syk (21, 22), which further transduces signaling via activation of the membrane scaffolding protein LAT (26, 27). However, studies have shown that the protein-protein interactions that regulate FcεRI signaling can be influenced by antigen type. Mahajan et al showed that the recruitment of SHIP1 can be modulated with DF3 stimulation, where doses of DF3 that resulted in reduced degranulation (high-dose inhibition) showed increased recruitment of phosphorylated SHIP1 to FcεRI aggregates compared to optimal degranulation doses (6). More recently, we showed that removal of SHIP1 from FcεRI aggregates by CRISPR-mediated knockout enhanced Syk binding lifetime. This resulted in increased Syk phosphorylation, demonstrating that protein interaction dynamics regulate signal strength (25). Using the trivalent, rigid DNA antigens described above, Sil et al showed that while FcεRI phosphorylation and degranulation were dependent on the distance between haptens, signaling along the PLCγ axis was not (10). Suzuki et al compared FcεRI signaling induced by low (NP)- and high (DNP)-affinity antigens presented on a SLB and found that NP elicited reduced degranulation and cytokine production, but had enhanced chemokine secretion (15). These differences were attributed to the ability of NP to preferentially recruit the SFK Fgr over Lyn and the scaffold NTAL over LAT. Therefore, the organization of the FcεRI aggregate, as dictated by discrete antigens, directs the balance of positive and negative signaling regulators in the signalosome, ultimately fine-tuning the cellular response.

To better understand the underlying mechanisms connecting antigen-induced aggregate organization to differential signaling, we compared the response of the model cell line Rat Basophilic Leukemia-2H3 (RBL) primed with DNP-specific IgE (28) to either the multivalent antigen DNP-BSA or trivalent DF3. We show here that DNP-BSA is more efficient at inducing receptor phosphorylation and degranulation than DF3. The ability of FcεRI aggregates to recruit SHIP1 was found to be greater with DF3 activation, contributing to the reduced signaling. Furthermore, in the complete absence of Lyn, DF3 was unable to support degranulation at any dose. Using dSTORM super-resolution imaging and a novel image analysis algorithm, Bayesian Grouping of Localizations (BaGoL) (29), we mapped the spatial organization of receptor aggregates. We found nanoscale differences in the relative arrangement of DNP-BSA and DF3 aggregates, with DNP-BSA aggregates being larger in area and having a larger spacing between receptors than DF3 aggregates. Because other ITAM-bearing receptors have been shown to be regulated by conformational changes (30–32), we asked whether the above results could be explained by distinct conformational changes between FcεRI subunits. We measured Förster resonance energy transfer using fluorescence lifetime imaging microscopy (FRET-FLIM) to monitor proximity between the receptor subunits and found that crosslinking with DNP-BSA reduced the proximity between subunits more than DF3, linking conformational changes to signaling efficiency. Similar FRET changes were seen between receptor subunits at the mast cell synapse as FcεRI engages with monovalent antigen presented on an SLB. Finally, we identified a role for force in optimizing FcεRI signaling. Immobilizing DF3 on a rigid surface alters the signaling profile of RBL-Lyn^{KO} cells, inducing a small, but significant, dose-dependent degranulation response. Consistent with this finding, we show that activating RBL-WT cells with a custom-made DNP-PEG$_{12}$-BSA that contained flexible PEG$_{12}$ linkers resulted in reduced mast cell secretion compared to DNP-BSA. Together, these results suggest a highly complex

interplay of mechanisms that are influenced by the distinct properties of individual antigens, to tune FcεRI signal strength and regulate mast cell outcomes.

Materials and Methods

Antibodies, Antigens, and Reagents

MEM media was purchased from Life Technologies (Grand Island, NY). G418 Disulfate was obtained from Caisson Labs (G030-5GM). Fura-2AM was purchased from Molecular Probes (Eugene, OR). DNP_{25}-BSA was from ThermoFisher Scientific (Waltham, MA; catalogue #A23018), custom DF3 peptide synthesized by and purchased from Anaspec (Fremont, CA) and anti-DNP-IgE was affinity-purified from ascites (Covance, Denver, PA) according to the methods of Liu et al (28). AlexaFluor647- (Thermofisher Scientific #A-20006), Janelia Fluor 646- (Tocris #6148) and CF640R- (Biotium #92108) labeled IgE lots were prepared using NHS Ester conjugation. Antibodies used are listed as follows: anti-pY PY20/99 cocktail (SantaCruz; sc-508, sc-7020), anti-rabbit-HRP secondary (SantaCruz; sc-2004, Cell Signaling #7074), anti-FcεRIγ (EMD Millipore; 06-727), Goat anti-rat IgE (Abnova; PAB29749). Poly-L lysine was purchased from Sigma-Aldrich (P1524-100MG), 18:1 (Δ9-Cis) PC (DOPC) and 16:0 DNP Cap PE lipids were purchased from Avanti Polar Lipids (850375C and 810528C, respectively). DNP-Peg12-NHS ester was purchased from BroadPharm (BP-22397). All live-cell RBL imaging was performed in modified Hank's buffered salt solution (additional 10 mM Hepes, 0.05% w/v BSA, 5.45 mM glucose, 0.88 mM $MgSO_4$, 1.79 mM $CaCl_2$, 16.67 mM $NaHCO_3$).

Cell Culture

We utilized RBL-γ^{KO}, RBL-Lyn^{KO}, RBL-Lyn-γ^{dKO}, and RBL-$SHIP1^{KO}$ CRSPR-edited cell lines as described in previous work (25, 33). All RBL-2H3 cell variants (34, 35) were cultured in MEM media supplemented with 10% heat-inactivated fetal bovine serum, puromycin, and l-glutamine. Plasmid transfections were performed using the Amaxa system (Lonza) with Solution L (Lonza VCA-1005 or MirusBio Ingenio solution MIR-50114) and Program T-020. For all microscopy experiments, cells were plated overnight into eight-well Lab-Tek (Cellvis; c8-1-n) chambers at a density of $4x10^5$ cells/well or a 6 well tissue-culture plate (Fablab) on round cover glass, #1.5h thickness, 25 mm (Warner Instruments) at a density of $2x10^5$ cells/well and primed overnight with either fluorescently-labeled or dark IgE, as appropriate.

Plasmid Constructs

Generation of Syk-mNG and SHIP1-mNG were described previously (25, 36). The FcεRI-β and FcεRI-γ constructs referred to rat DNA and consisted of the respective DNA being fused to mNG, mEGFP or mScarlet via a short linker (GGTGGAGGCGGTAGC) and generated via fusion PCR. Total cDNA for all constructs were amplified by PCR before subcloning into the pcDNA3.1 directional topo vector (Life Technologies). All constructs were checked by Sanger sequencing (GENEWIZ).

Western blot analysis

Cells ($5x10^6$) were plated on 100-mm tissue-grade culture plates and primed overnight with 0.5 μg/mL IgE. Cells were stimulated with respective antigen or mock for indicated times at 37°C in

modified Hank's buffered saline. Cells were rinsed in ice-cold PBS and lysed on ice for 30 min with NP-40 lysis buffer (150 nM NaCl, 50 mM Tris, 1% NP-40) in the presence of Halt Protease and Phosphatase inhibitors (Thermo Fisher Scientific #78446). Lysates were cleared by centrifugation at 11,000 x g for 20 min at 4°C. Cell lysates were immunoprecipitated by first incubating lysates with the anti-IgE antibody on a rotator, at RT for 1 hour. Protein A/G PLUS-Agarose (Santa Cruz; sc-2003) beads were added after initial antibody incubation and samples were then incubated again at 4°C overnight with rotation. Samples were then washed via centrifugation (2500xg for 3 minutes at 4°C) three times with NP-40 lysis buffer, in the presence of Halt Protease and Phosphatase inhibitors. Samples were boiled in 2x non-reducing sample buffer (BioRad; 1658063). After centrifugation and removal of beads from boiled samples, they were analyzed via immunoblotting. Proteins were separated via SDS-PAGE electrophoresis (4-20% gel; Biorad 4568093) and transferred to nitrocellulose membranes using the iBlot2 system (Life Technologies). Membranes were blocked for 30 min in 3% BSA-0.1% Tween-20-Tris Buffered Saline (BSA-TBST) and probed overnight with primary antibodies at 4°C. HRP-conjugated secondary antibodies were used for detection and incubated with membranes for 1 hour at room temperature. Membranes were imaged on the Odyssey FC2 Imager (Li-COR Biosciences) after incubation with Supersignal West PICO plus (Thermo Fisher Scientific #34580). Resulting densitometry images were analyzed with ImageStudio Software.

Degranulation Assays

$2x10^5$ cells/well were plated in 24-well tissue culture plates, along with 0.5 µg/mL IgE, for 24 h. Cells were washed and stimulated in Hank's buffer with indicated concentration of DNP-BSA, DF3 or DNP-Peg12-BSA for 30 min at 37°C. Percent release of granular contents was measured by β-hexosaminidase concentration as previously described (36). For immobilized DF3 degranulation, 24 well TC plates were coated with Poly-L-lysine solution (Sigma-Aldrich; P4707), allowed to dry fully and then incubated overnight with respective antigen solution. 1XDF3 in figure refers to 100 nM. Before degranulation, immobilized DF3 plates were washed 5 times with PBS to remove free antigen. $4x10^5$ cells were then plated onto immobilized antigen wells and incubated for 30 min at 37°C. Supernatant was collected and centrifuged to remove free floating cells before proceeding with the protocol as described previously (37).

Fura-2AM Calcium Assay

In all cases, cells were washed with Hanks buffer and ratio images were acquired at 35°C using an Olympus IX71 inverted microscope outfitted with a UPLANSAPO 60X/NA1.2 water immmersion objective coupled to an objective heater (Bioptechs). Cells were activated by cross-linking with DNP-BSA, added exactly at 30 seconds into a total of 5 min of imaging. Ratiometric changes in cytosolic calcium were determined by alternating between 340 and 380 nm excitation at 1 Hz with a xenon arc lamp monochromator (Cairn Research OptoScan) and collecting the interleaved Fura-2 fluorescence emissions at 510 nm with an iXon 887 EMCCD camera using IQ3 imaging software (Andor Technology). Offline single-cell (15-40 per field of view) ratiometric analysis was performed with custom MATLAB scripts to assess reported properties of calcium release (36).

Preparation of DNP-SLB

DNP-SLB surfaces were prepared as described in (14). Briefly, we composed mixed liposomes containing 18:1 (Δ9-Cis) PC (DOPC) and 16:0 DNP Cap PE lipids at the listed ratio. These were heated to 37°C and added to surfaces cleaned with piranha solution (3:1 H_2SO_4:H_2O_2). SLB fluidity was confirmed after bilayer formation via fluorescence recovery after photobleaching (FRAP) after fluorescently labeling an SLB with a lipid-intercalating dye.

FLIM-FRET Imaging and Analysis

Fluorescence Lifetime images were obtained using a Leica DMi8 inverted microscope and a PicoHarp 300 time correlated single photon counting (TCSPC) module plus picosecond event timer (PicoQuant GMBH Berlin, Germany #973001). A Leica Harmonic Compound PL apochromatic CS2 63X water objective with a correction collar (1.2 NA) was used for imaging. Cells were imaged at 35°C with temperature maintained using a Bioptics Objective heater. A tunable White Light Laser (470 - 670 nm) with 4% laser power and a 488 nm notch filter (donor excitation) and 561 nm notch filter (acceptor excitation) was used to excite samples with a pulse rate of 80 mHz. A scan speed of 700 and a 256x256 resolution was used. Two hybrid detectors collected photons at (498-532 nm) and (608-650 nm) respectively on the photon counting mode setting, with only the 488 notch filter active and the 498-532 hybrid detector active during FLIM acquisition. Fluorescence decay rate was measured over 20-25 laser pulse repetitions and the data was fit to either one or two component reverse exponential equations using Symphotime 64 software (PicoQuant) to calculate average lifetime. An intensity-based threshold was employed to discern between receptors in aggregates and receptors outside aggregates. Imaging was performed at the basal membrane.

dSTORM Super Resolution Cell Fixation and Imaging

RBL-WT cells were plated on piranha-etched 25 mm coverslips at single-cell densities and labeled overnight with 1 µg/mL IgE-AF647. Prior to treatment, cells were washed three times with warm Hank's buffer to remove any unbound IgE-AF647. Stimulation at the indicated concentration of DNP_{25}-BSA or DF3 was completed in Hank's buffer for 5 min at 37°C. Cells were then quickly fixed by dunking coverslips in cold 1x phosphate buffered saline (PBS) and immediately submerged in 100% -20˚C methanol for at least 30 min. Cells were rehydrated in 1x PBS for at least 30 min after removal from methanol and subsequently washed with 1x PBS three times. Sample were imaged the same day as fixation using standard dSTORM imaging buffer with an enzymatic oxygen scavenging system and primary thiol: 50 mM Tris, 10 mM NaCl, 10% w/v glucose, 168.8 U/ml glucose oxidase (Sigma #G2133), 1404 U/ml catalase (Sigma #C9322), and 60 mM 2-aminoethanethiol (MEA), pH 8.0. Data were collected using a custom-built microscope (38) equipped with a 1.35 NA silicon oil immersion objective and an sCMOS camera (C11440-22CU; Hamamatsu Photonics) (Olympus UPLSAPO100XS). A 647 nm laser was used for excitation (500 mW 2RU-VFL-P; MPB Communications Inc.) and emission was collected with a 708/75 nm filter (FF01-708/75-25; Semrock). A total of 60,000 frames were collected per cell with an exposure time of 50 ms per frame. Images were registered every 10,000 frames (38)

dSTORM Image Reconstruction

dSTORM images were analyzed and reconstructed with custom-built MATLAB functions that are available as part of the *smite* package (https://github.com/lidkelab). Briefly, for each image frame, sub-regions were selected around local maxim that were above a threshold. Each sub-region was fit using a finite pixel Gaussian point spread function using a maximum likelihood estimator (39). Fitted results were rejected using a log-likelihood ratio test (40). The fit precision was estimated using the Cramér-Rao lower-bound values for each parameter. Blinking events that spanned multiple contiguous frames were found and connected using the cost matrix approach described in (41). The resulting coordinates were corrected for sample drift by minimizing pairwise distances as described in (42).

BaGoL Emitter Fitting Method

Coordinate data from dSTORM imaging was post-processed using the using the BaGoL (Bayesian Grouping of Localizations) algorithm which has been previously described (29). Briefly, the BaGoL grouping method is implemented in MATLAB as part of the *smite* single molecule analysis package. It functions to group coordinates from multiple blinking events into estimates of the true number and locations of the underlying emitters. This process improves the precision of the estimate of the emitter locations and facilitates downstream analysis. The parameters for the BaGoL analysis used for this data set were: Length of burn-in chain 64,000; number of trials 16,000; ROI size 500 nm; SE adjust 5 nm; initial blinking distribution Xi [20,1].

DBSCAN Cluster Analysis

Analysis of dSTORM FcεRI aggregation data was performed using the density-based DBSCAN algorithm implemented in MATLAB as part of a package of local clustering tools (https://stmc.unm.edu/) (43, 44). Parameters chosen were a maximal distance between neighboring cluster points of $\varepsilon = 60$ nm and a minimal cluster size of three observations. Cluster boundaries were produced with the MATLAB “boundary” function using a default methodology that produced contours halfway between a convex hull and a maximally compact surface enclosing the points. ROIs of size 3.0 µm × 3.0 µm (9.0 μm^2) were selected from the set of images from which statistics for the circularity, NND, and area were collected per cluster. Circularity (sometimes known as compactness) is defined as $(\pi * A) / p^2$; where A is the area of the cluster and p is the perimeter.

TIRF Microscopy Optical Setup for 2 Color Imaging and Correlation

All TIRF imaging data was collected using an inverted microscope (IX83; Olympus) equipped with a 60×/1.5 NA oil-immersion TIRF (UPlanApo; Olympus) and included a correction collar, with an additional 1.6X magnification applied (total 100X magnification). Fluorescent excitation used a 640 nm/140 mW diode laser (Olympus Soft Imaging Solution; 00026121) and a 488 nm/100mW diode laser (Olympus Soft Imaging Solution; 00026125). Images were captured using a Hamamatsu ORCA-Fusion sCMOS camera (C14440) and Hamamatsu W-View Gemini image splitter (A12801-01). For simultaneous 2-color, live cell acquisition a filter set of Chroma single-bandpass 705/100 nm (394148) and a Semrock 520/28 nm (FF02-520/28) were used in combination with a Semrock single-edge standard epi-fluorescence dichroic beamsplitter

(FF555-Di03). Images were acquired at 900 ms exposure time. Samples were held at 36°C using a Bioptechs objective heater controller (150803).

BAMF Image Analysis

We used Bayesian Multiple-emitter Fitting (BAMF) (25, 45) to process the acquired raw image frames of IgE and SHIP1 and localize the emitters as well as classifying them into signal (in-focus) and background (out-of-focus) emitters. The signal emitters found by BAMF were used to reconstruct background/noise free images of IgE. The obtained noise free images of IgE were then used to find the borders of IgE clusters using a Sobel filter for edge detection. Given the edges of the IgE clusters, we found the SHIP1 molecules that reside inside each IgE cluster. The technique used to identify emitters inside the borders of IgE clusters is as follows: An emitter location happens to be outside a closed border with a convex shape if all the coordinates of the border are either smaller or larger than the emitter location. Otherwise, the emitter is located inside the borders. Eventually, the SHIP1 intensity associated to each IgE cluster intensity was found by the sum of the intensities of found SHIP1 locations inside those borders. At the end, the intensity of the IgE clusters were plotted against the intensity of the corresponding SHIP1 molecules to find the correlations.

Statistical Analysis

Analysis of calcium data and super-resolution images was performed using in-house MATLAB code as described above. All statistical tests for comparisons between groups was performed using Graphpad Prism version 0.9.0.0, with the exception of the Bernoulli Trial analysis that was performed in Microsoft Excel.

Results

Antigen properties modulate FcεRI signaling outcomes

We began by comparing the ability of trivalent DF3 and multivalent DNP-BSA to induce mast cell degranulation. DNP-BSA is a commonly used allergen mimic that contains a Poisson distributed number of DNP haptens on the surface and is known to induce a high degree of receptor crosslinking and robust mast cell responses (46, 47). For the experiments described here, DNP-BSA was determined to have a Poisson averaged valency of 14 (see Methods). Using our model mast cell system, RBL cells primed with anti-DNP IgE (28), we found that trivalent DF3 produced degranulation with a bell-shaped dose curve (Fig 1A, gray bars) that peaks at 10 nM DF3. This result is consistent with our previous work that first characterized the antigen (6). In contrast, the dose response curve for crosslinking by DNP-BSA is already maximal at 0.14 nM and the levels remain high as dose increases (Figure 1B, gray bars). Differences in cellular response became even more evident when we compared degranulation in cells lacking the SFK Lyn. We recently showed that DNP-BSA can override the need for Lyn, as evidenced by the ability of DNP-BSA to induce degranulation in RBL cells where Lyn was knocked out by CRISPR/Cas9 gene editing (RBL-Lyn^{KO}; (25)). Figure 1B shows that the dose response for DNP-BSA is nearly the same for RBL-WT and RBL-Lyn^{KO} cells, even at very high doses. Remarkably, DF3 was not able to support degranulation in RBL-Lyn^{KO} cells at any dose (Fig 1A, red bars).

One of the earliest signaling outcomes after FcεRI crosslinking is an increase in intracellular calcium levels, a requirement for degranulation (48). Therefore, we next tested the ability of DF3 to induce calcium flux in RBL-WT and RBL-Lyn^{KO} cells. Cells were loaded with the Fura-2 calcium dye and imaged and quantified as described previously (36). Heatmaps in Figures 1C &

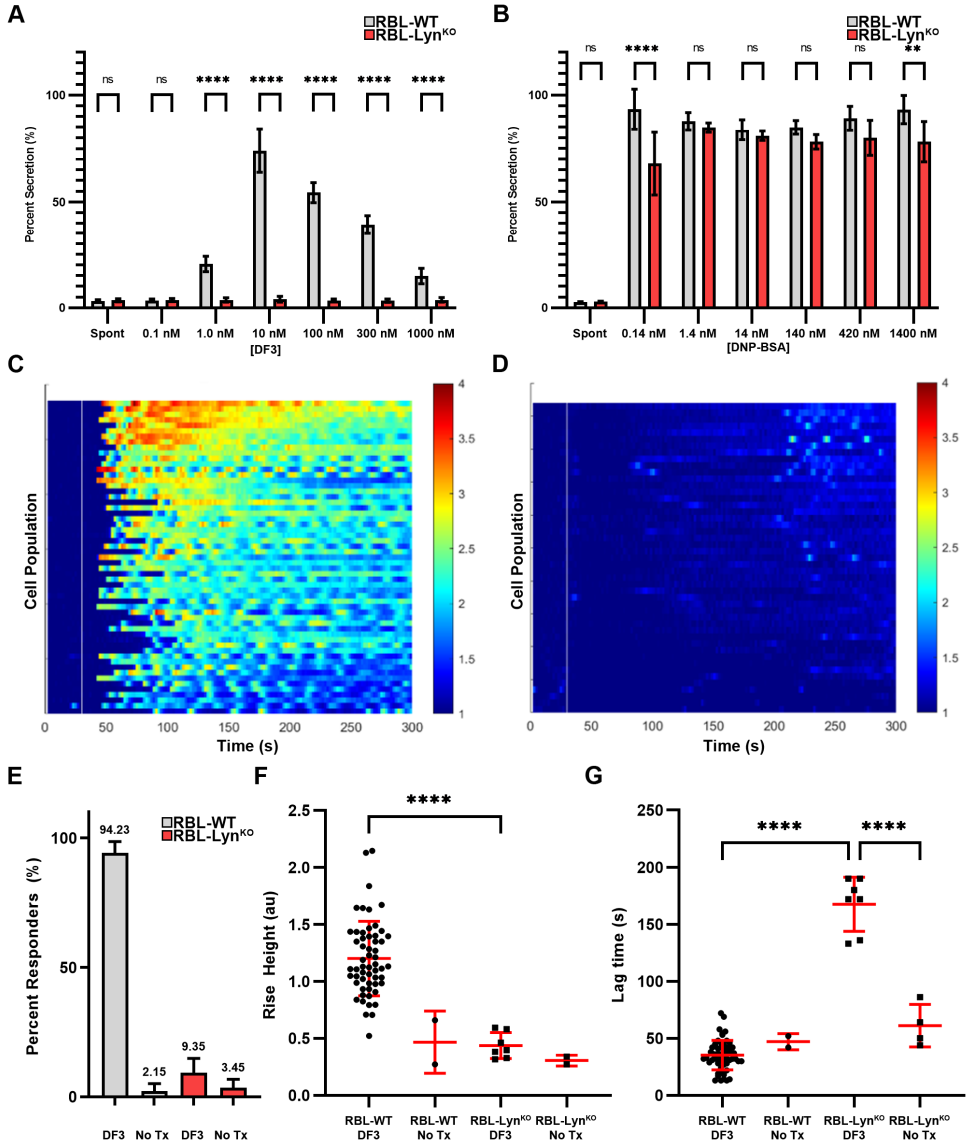

Figure 1. DNP-BSA and DF3 induce differential mast cell outcomes. A,B) Degranulation results from RBL-WT or RBL-Lyn^{KO} cells. Cells were incubated overnight with saturating IgE before 30 min of activation with DF3 (A) or DNP-BSA (B) at the listed concentrations. Error bars represent SD. n=9 wells across s 3 replicate experiments. **C,D)** Calcium release in RBL-WT (C) or RBL-Lyn^{KO} (D) cells after antigen activation with 10 nM DF3; n=104 and n=107, respectively. Kymographs display the Fura-2 ratio over time on a heatmap, where each row represents a single cell response. **E)** The percent of total cells which released detectable calcium for cells treated with 10 nM DF3 or with addition of Hank's buffer (No Tx) for both RBL-WT and RBL-Lyn^{KO} cells. Error bars display 95% confidence interval calculated by Bernoulli trial analysis. **F,G)** Quantification of the initial magnitude of calcium released (Rise Height, F) and the delay between antigen addition and calcium flux (Lag Time, G). **** $p<0.0001$, Two-way ANOVA with Sidak's multiple comparison test.

D depict the Fura-2 ratio over time as cells are stimulated, where each row represents a single cell response. Crosslinking with 10 nM DF3 in RBL-WT cells produced a robust calcium response (Fig 1C). In contrast, the response in RBL-Lyn^{KO} cells with the same antigen and dose was barely detectable (Fig 1D) over unstimulated control cells (Figure S1), consistent with the inability to induce degranulation (Fig 1A). Notably, only ~ 9% of RBL-Lyn^{KO} cells recorded any detectable calcium response with 10 nM DF3 activation, while DNP-BSA activation resulted in ~ 94% cellular response (Fig 1E). Comparing the magnitude and timing of the cells that did respond shows that RBL-WT cells have a higher maximal calcium flux (Fig 1F) that occurs more rapidly (Fig 1G) than for RBL-Lyn^{KO} cells. While the fraction of RBL-Lyn^{KO} cells that responded to DF3 stimulation was slightly increased over unstimulated cells, the magnitude of calcium flux was not significantly higher. Therefore, DF3 is unable to support FcεRI signaling in the absence of Lyn.

DF3-induced high dose inhibition is related to enhanced SHIP1 recruitment

We next compared secretion capability between RBL-WT and RBL cells lacking the negative regulator SHIP1 (RBL-SHIP1^{KO}). Mahajan et al showed that the knockdown of SHIP1 using siRNA resulted in an increase in degranulation at all doses, but the high dose inhibition remained (6). Here, we found that complete knockout of SHIP1 using CRISPR/Cas9 gene editing (25) abrogated high-dose inhibition (Fig 2A, red bars). Knockout of SHIP1 did not alter the DNP-BSA dose response (Fig 2B). This result suggests that the activity of SHIP1 is more sensitive to DF3-induced aggregation than that of DNP-BSA. To understand if aggregate geometry can modulate SHIP1 recruitment, we expressed SHIP1-mNG in RBL-SHIP1^{KO} cells and quantified the recruitment of SHIP1-mNG to IgE-CF640R-labeled FcεRI aggregates. Cells were imaged using Total Internal Reflection Fluorescence (TIRF) microscopy after 5 min of activation with 1000 nM DF3 or 1400 nM DNP-BSA (Fig 2C, D). Figure 2E plots the individual aggregate size (IgE-CF640R intensity) against the intensity of SHIP1-mNG recruited to that aggregate (see also Figure S2), using the Bayesian Multiple-emitter Fitting (BAMF) method as described previously (25, 45). We did find significant association of SHIP1 structures with the membrane of resting cells (Figure S2), consistent with the fact that it contains multiple binding motifs, including PH- and C2-domains, that facilitate interaction with a variety of signaling molecules. We generated our mask on IgE-CF640R signal to ensure that the focus is on SHIP1 recruited to activated FcεRI. We found that the amount of SHIP1 recruited to DF3 aggregates (blue) is consistently greater than that for DNP-BSA aggregates (orange). At this high dose of antigen, the distribution of FcεRI aggregate intensities was the same for each antigen, indicating that aggregate size does not explain the observed difference in SHIP1 recruitment. These results, along with the above observations seen in RBL-Lyn^{KO} cells, demonstrate that antigen size, valency, and/or epitope spacing can modulate the balance of positive and negative signaling to affect mast cell outcomes.

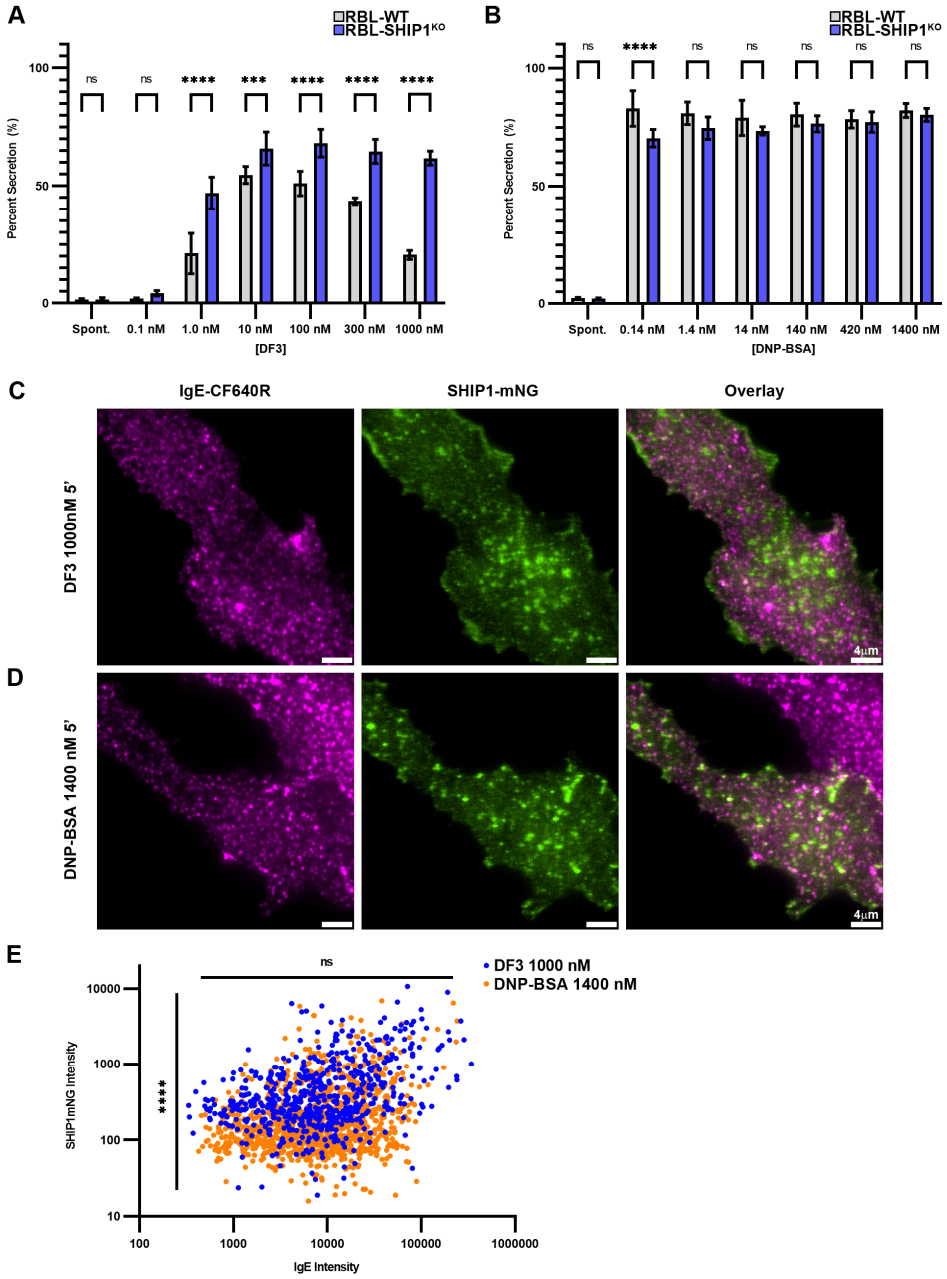

Figure 2. DF3-induced high-dose inhibition is a result of SHIP1 recruitment to FcεRI clusters. A,B) Degranulation results from RBL-WT or RBL-SHIP1^{KO} cells. Cells were incubated overnight with saturating IgE before 30 min of activation with DF3 (A) or DNP-BSA (B) at the listed concentrations. Error bars represent SD. n=9 wells across 3 replicate experiments. *** $p<0.001$, **** $p<0.0001$, Two-way ANOVA with Sidak's multiple comparison test. **C,D)** Representative images of RBL-SHIP1^{KO} cells reconstituted with SHIP1-mNG (green) and primed overnight with IgE-CF640R (magenta), acquired in TIRF. Cells were maintained at 37°C during imaging and activated with high doses of each antigen: 1000 nM DF3 (C) or 1400 nM DNP-BSA (D) for 5 minutes. **E)** Quantification of the amount of SHIP1-mNG recruited to individual FcεRI aggregates, plotted as the IgE-CF640R intensity versus SHIP1-mNG intensity per aggregate (see BAMF Image Analysis). n = 598 aggregates (DF3) and 1088 aggregates (DNP-BSA) acquired over 6 cells each. **** $p<0.0001$, Welch's unpaired t-test comparing SHIP1-mNG intensities and IgE intensities between antigenic conditions, respectively.

Antigen properties dictate FcεRIγ phosphorylation levels

Because recruitment of signaling molecules to FcεRI depends on ITAM phosphorylation, we next sought to determine if antigens can differentially modulate the phosphorylation state of the receptor itself. RBL-WT, RBL-Lyn^{KO}, or RBL-SHIP1^{KO} cells were stimulated with optimal antigen doses for 8 min, then lysed and FcεRIγ phosphorylation was probed by western blot. The receptor complex was immunoprecipitated using an anti-IgE antibody and prepared under non-denaturing conditions to retain an intact FcεRI γ-dimer that separates on the gel by phosphorylation state (25, 49). Figure 3A shows a representative western blot, probed for phosphotyrosine (pY), where the FcεRIγ phosphorylation pattern is seen as four bands (1-4

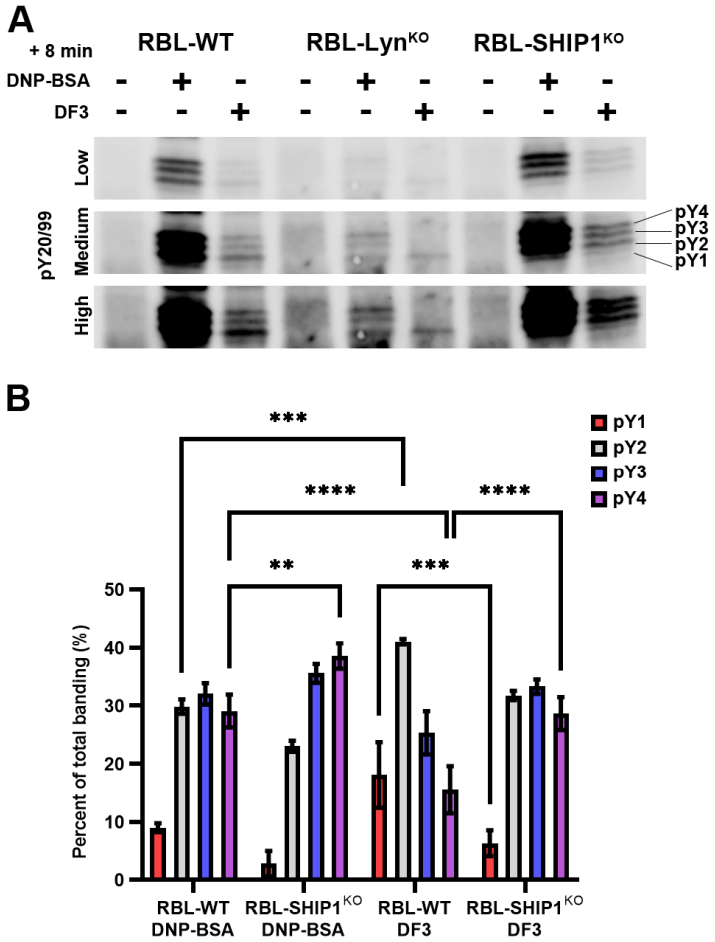

Figure 3. FcεRIγ phosphorylation is stronger and more complete with DNP-BSA over DF3. A) Whole cell lysates were collected from RBL-WT, RBL-Lyn^{KO} or RBL-SHIP1^{KO} cells at rest or after DNP-BSA (14 nM) or DF3 (10 nM) crosslinking for 8 min. The 8 min time point was chosen to match peak pY observed previously in RBL-Lyn^{KO} cells (25). Phosphorylation-induced banding was visualized via western blotting with anti-pY20/99 antibody cocktail. Representative western blot is displayed with different contrasts (low, medium, high) to allow visualization of conditions with lower phosphorylation levels. **B)** Densitometry quantification of immunoblots described in (A). Bars represent the percentage contribution of each γ-ITAM-dimer phosphorylation state to the total FcεRIγ activation profile. n=3 independent experiments, ** $P < 0.01$, *** $P < 0.001$, **** $P < 0.0001$, Two-way ANOVA with Tukey's multiple comparison's test.

possible phosphotyrosines per dimer; pY1, pY2, pY3, pY4). Notably, the total γ-pY signal for DF3 stimulation is consistently lower than that of DNP-BSA. Further quantification of the γ-pY banding seen in Figure 3B shows that DF3 has a less complete phosphorylation profile, not reaching the pY3 and pY4 levels to the same extent as DNP-BSA, across all cell lines. Consistent with the enhanced degranulation seen with DF3 in RBL-SHIP1^{KO} cells, the γ-pY is shifted from pY2 to the more complete pY4 in SHIP knockout cells. Therefore, antigen attributes directly influence the efficiency of receptor phosphorylation.

Signaling efficiency is correlated with aggregate geometry

Considering that antigens are able to dictate receptor phosphorylation, we postulated that the nanoscale organization of the aggregate plays a role in signaling efficiency. However, it has been challenging to characterize aggregates due to their small size, which is below the diffraction limit of light. Super-resolution imaging, such as single molecule localization microscopy (SMLM) techniques, provides sub-diffraction information, but the repeated blinking of fluorophores has made it difficult to identify discrete single emitters (50, 51). Recently, Fazel et al developed an analysis algorithm that increases the precision obtained in SMLM by grouping repeat localizations from the same emitter (29). This is achieved using Bayesian statistics to perform a weighted average over all possible groupings, ultimately assigning multiple blinking events to their respective emission source. This algorithm, termed Bayesian Grouping of Localizations (BaGoL), results both in increased localization precision (6.72 +/- 1.89 nm) and enables the identification of individual emitters (see Figure S3). We used dSTORM imaging of IgE-AF647-labeled FcεRI (36, 52) combined with BaGoL analysis to accurately map the organization of individual FcεRI aggregates. Figure 4 shows representative BaGoL images and DBSCAN (43) aggregate cluster contours for RBL-WT cells stimulated for 5 min with optimal doses of either DNP-BSA (Fig 4A) or DF3 (Fig 4B). Aggregates formed by DF3 crosslinking are smaller in area compared to DNP-BSA (Fig 4C). Both DNP and DF3 aggregates have a broad distribution of shapes, as measured by circularity (see Methods), ranging from more linear (circularity close to 0) to nearly round (circularity close to 1) (Fig 4D). Even though the median circularity values are similar, DF3 has a higher fraction of more linear structures. We also calculated the nearest neighbor distances (NND) between receptors within aggregates and found that the receptors are more closely packed in DF3 aggregates (Fig 4E). These results demonstrate that FcεRI activation is sensitive to nanoscale differences in aggregate geometry that is itself due to differences in antigen structure.

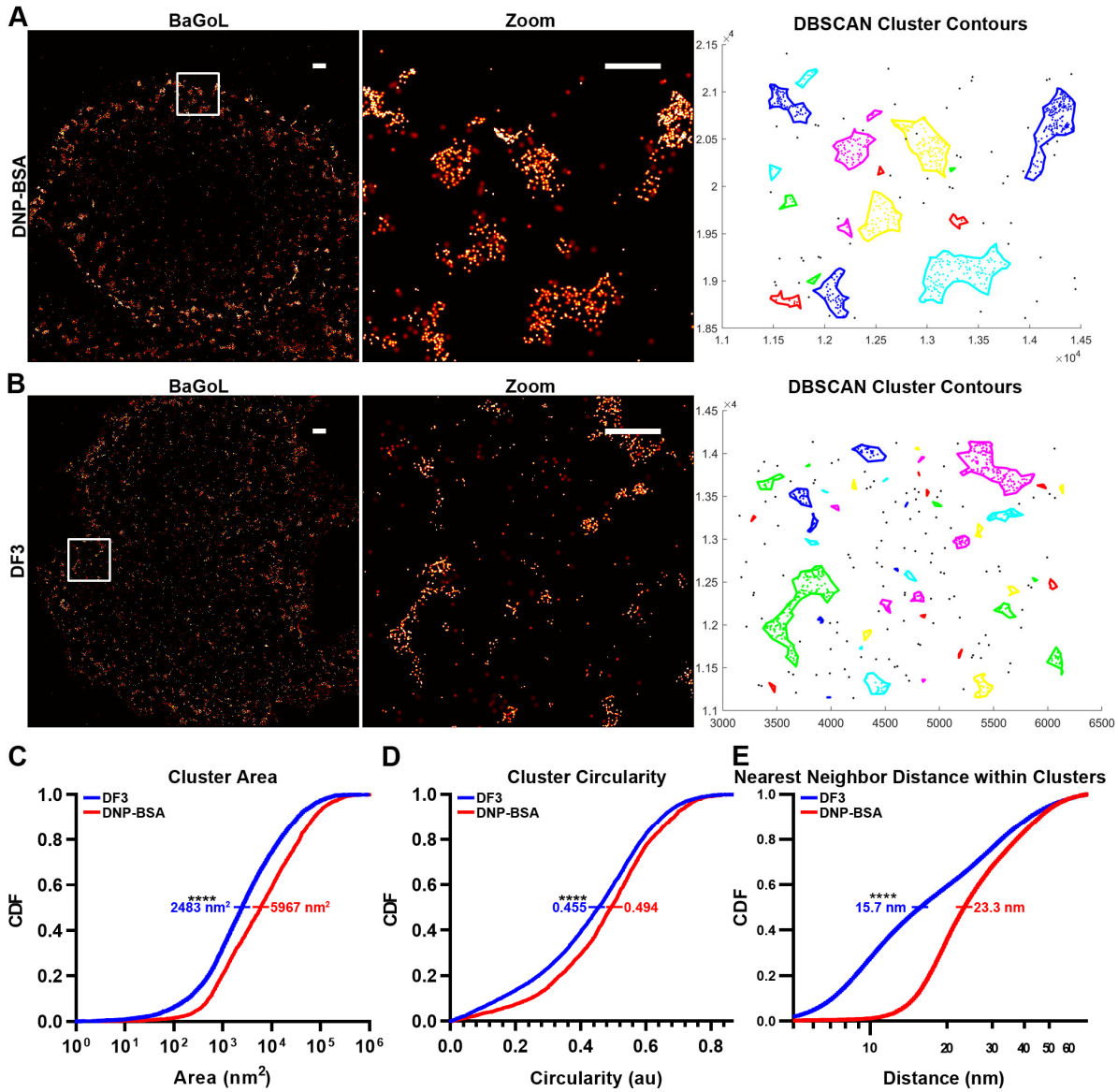

Figure 4. Nanoscale organization of FcεRI aggregates. A,B) Representative super-resolution imaging of 14 nM DNP-BSA (A) and 10 nM DF3 (B) aggregates after 5 min of crosslinking. Left: Single cell images of BaGoL-collapsed dSTORM localizations, Middle: 4x magnification of ROI (white box), and Right: DBSCAN clustering of BaGoL-localized emitters within the ROI. Scale bars, 500 nm. **C,D,E)** Quantification of aggregate properties from DBSCAN analysis, represented as cumulative distribution functions (CDF). **C)** Aggregate area, **D)** Aggregate circularity and **E)** receptor to receptor spacing (nearest neighbor distance, NND) within aggregates. **** $P < 0.0001$, analyzed by Kolmogorov-Smirnoff Test. n = 2447 aggregates for DNP-BSA and 6887 for DF3 (D, E) or n = 42,632 calculated receptor spacings for DNP-BSA and 78,730 for DF3 (F), acquired over 6 cells for each condition.

DNP-BSA and DF3 elicit different FcεRI conformational changes

We next wondered how the change in aggregation translates to the tuning of FcεRI function. Based on evidence showing other ITAM-bearing receptors are regulated by structural changes (30–32, 53), we hypothesized that FcεRI signal initiation is associated with conformational changes. To measure receptor conformation, we developed a FRET system to monitor the relative proximity between receptor subunits: β-mEGFP (donor) to γ-mScarlet (acceptor), or γ-

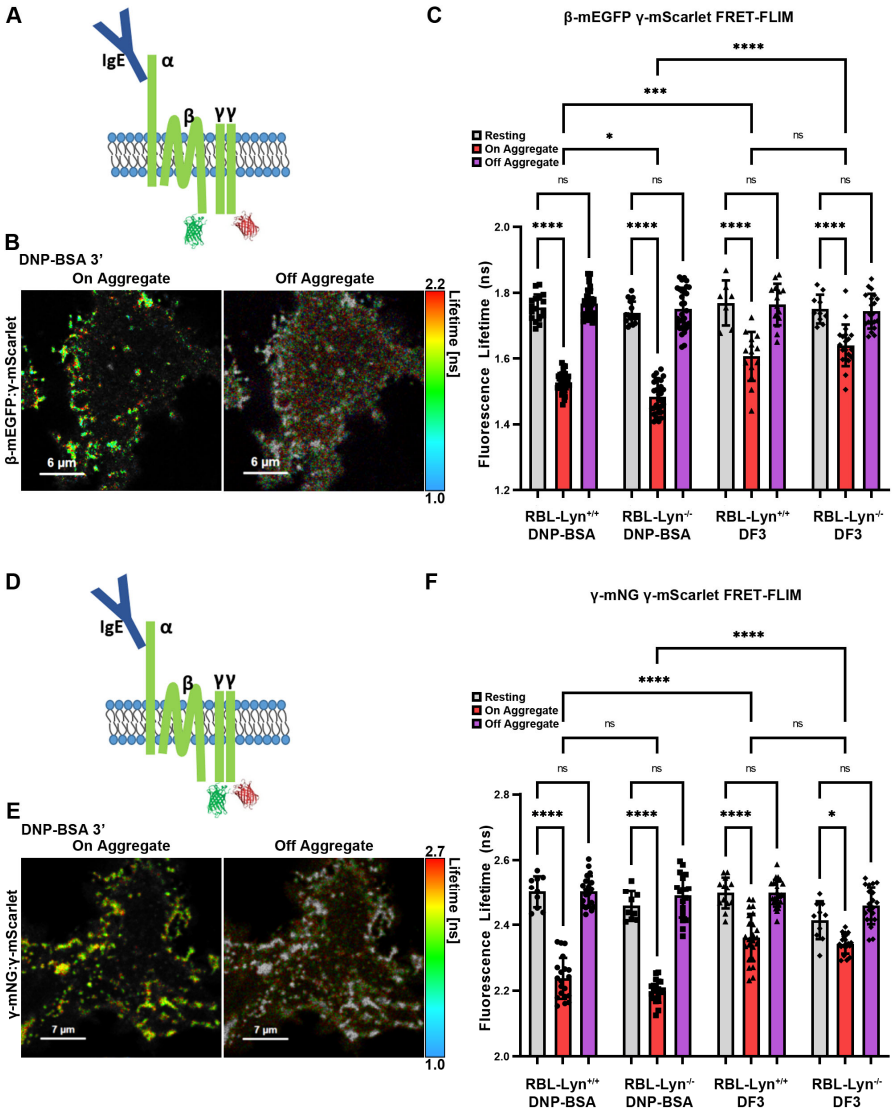

Figure 5. FcεRI aggregation induces receptor conformational changes that vary with antigen. A) Cartoon depicting location of fluorophores on receptor subunits: β-mEGFP (donor, green) and γ-mScarlet (acceptor, red). **B)** Representative lifetime images showing "on aggregate" (left) and "off aggregate" (right) masking of a cell after activation with 14 nM DNP-BSA. **C)** Quantification of fluorescence lifetimes (τ_{DA}) in resting cells and cells activated with 14 nM DNP-BSA or 10 nM DF3. Lifetimes were compared between cells with ($Lyn^{+/+}$) and without ($Lyn^{-/-}$) endogenous Lyn. Reductions in average τ_{DA} indicate relative increase in FRET. **D)** Cartoon depicting receptor γ-subunit labelled with either mNG (donor, green) or mScarlet (acceptor, red). **E)** Representative lifetime images for γ-γ FRET measurements, similar to (B). **F)** Quantification of fluorescence lifetimes (τ_{DA}), similar to (C) but between γ-subunits. * $P < 0.05$, **** $P < 0.0001$. Two-way ANOVA with Tukey's multiple comparison test. 9-21 cells were imaged per condition across 3 replicate experiments. Each symbol in (C,F) represents a single cell measurement.

mNG (donor) to γ-mScarlet (acceptor) (Fig. 5A, C, respective cartoons). We measured FRET-induced changes in the donor lifetime (τ_D) when in the presence of acceptor (τ_{DA}) using FRET-FLIM (54–56). We began by examining the proximity of β-mEGFP and γ-mScarlet co-expressed in RBL-γ^{KO} cells (25, 33), such that all γ-subunits contained an acceptor. The τ_D for cells expressing β-mEGFP alone was 2.19 +/- 0.02 ns, consistent with previous reports (57). Co-expression of γ-mScarlet reduced the mEGFP lifetime (τ_{DA} = 1.75 +/- 0.04 ns) in resting cells, indicating energy transfer between the β- and γ-subunits. After crosslinking, we masked the aggregates in the FLIM images to compare τ_{DA} values 'on aggregate' and 'off aggregate' (Fig 5A, left and right images, respectively). τ_{DA} was found to be further reduced inside the aggregates (Fig 5B), for both DNP-BSA and DF3 activation, indicating that FRET is increased between β- and γ- subunits within active aggregates (Fig 5B). Interestingly, the amount of FRET was higher within DNP-BSA than DF3 aggregates. Outside of aggregates, τ_{DA} was unchanged from resting cells. In previous work, we showed that the β-subunit is not phosphorylated in cells that lack Lyn, and γ-phosphorylation is also significantly reduced (Figure 1 and (25)). We co-transfected the β-γ FRET pair into RBL cells lacking both Lyn and γ (RBL-Lyn/γ^{dKO}; (25)) to understand if ITAM phosphorylation is needed for the observed structural change. We found that FRET was again increased within aggregates for each antigen (Fig 5B), indistinguishable from RBL-WT cells. Therefore, the structural change is not strongly dependent on ITAM phosphorylation. Interrogation of FRET between the two γ-subunits showed similar trends (Fig 5D). Significant γ-γ FRET was observed in resting cells, with a change in lifetime between τ_D = 2.68 +/- 0.05 ns (58) and τ_{DA} = 2.47 +/- 0.06 ns. FRET was concomitantly increased inside of aggregates (Fig 5D), with DNP-BSA inducing a larger change in τ_{DA} than DF3. The detected FRET changes are likely not due to inter-receptor FRET because we see less FRET with DF3 where the receptor-receptor distance within aggregates was found to be smaller (Fig 4). Similar to β-γ FRET, the removal of Lyn did not alter γ-γ structural changes. For additional images, see Figure S4. These results indicate that crosslinking leads to FcεRI structural changes and that these changes do not require ITAM phosphorylation. Furthermore, there is a correlation between enhanced structural changes and more efficient signaling.

FcεRI undergoes a structural change when interacting with monovalent DNP-SLB

Previously, we have shown that mast cell degranulation can be induced upon engagement with monovalent-DNP embedded in an SLB (14). The mechanism driving FcεRI signaling in the absence of crosslinking was not clear; however we postulated that strain imposed on the receptor at the mast cell synapse may play a role in receptor activation. Thus, we performed FRET experiments similar to Figure 5 but instead examined subunit proximity upon engagement with a DNP-SLB. RBL-γ^{KO} cells expressing either the β-mEGFP/γ-mScarlet or γ-mNG/γ-mScarlet FRET pairs were dropped onto 20% DNP-SLBs and the forming synapse was imaged using FLIM. Figure 6 shows the comparison of the extent of FRET measured between either β-γ (Fig 6A) or γ-γ (Fig 6B) subunits for resting cells (adhered to glass coverslip) versus cells activated on a DNP-SLB. We found a significant decrease in τ_{DA} for receptors within the FcεRI synapse with both β-γ and γ-γ labeling. The relative reduction in lifetimes was more similar to DF3-induced aggregates than DNP-BSA (Fig 5), reflecting a less complete conformational change. To confirm that this conformational change was sufficient for signaling, we monitored

Syk recruitment to the synapse. RBL-WT cells expressing Syk-mNG, and primed with IgE-CF640R, were dropped onto DNP-SLBs and imaged at the adherent surface. Consistent with the ability of DNP-SLB to induce mast cell degranulation (14) we observed Syk-mNG recruitment to the FcεRI synapse (Fig 6C).

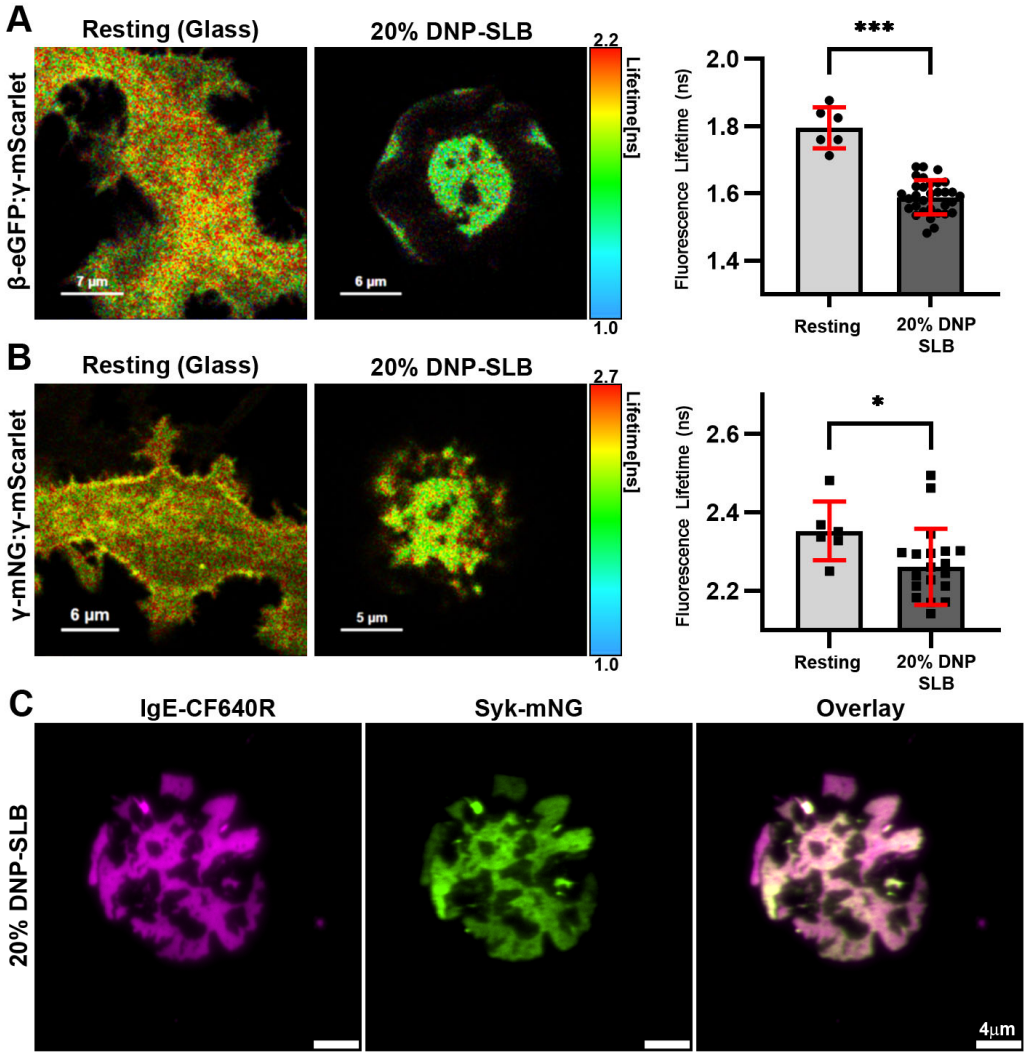

Figure 6. Receptor conformational changes occur within the mast cell synapse. A) Representative lifetime images of RBL-γ^{KO} cells expressing β-mEGFP:γ-mScarlet either plated on glass coverslips (Resting) or dropped onto 20% DNP-SLB coated coverslips. Right: Quantification of τ_{DA} in resting cells and within active mast cell synapses. Reduction in average τ_{DA} indicates relative increase in FRET. n = 32 activated cells and n = 6 resting cells across 3 independent experiments. **B)** Representative lifetime images of RBL-γ^{KO} cells expressing γ-mNG:γ-mScarlet either plated on glass coverslips (Resting) or dropped onto 20% DNP-SLB coated coverslips. Right: Quantification of τ_{DA} in resting cells and within active mast cell synapses. n = 20 activated cells and n = 6 resting cells across 3 independent experiments *** $P < 0.001$, * $P < 0.05$ Two-way ANOVA with Tukey's multiple comparison test. C**)** RBL-Syk^{KO} cells expressing Syk-mNG (green) and labeled with IgE-CF640R (magenta), interacting with 20% DNP-SLB and imaged using confocal microscopy. Representative image of n=20 total cells.

Forces play a role in FcεRI signal initiation

To confirm a role for mechanical forces in FcεRI signaling, we tested whether adding or removing strain would alter degranulation. We first introduced additional force by immobilizing DF3 on tissue culture plates so that the cells would experience the antigen presented on a rigid surface. Increasing amounts of DF3 were added to poly-L-lysine coated plates and incubated overnight. After washing away unbound DF3, RBL-WT or RBL–Lyn^{KO} cells were dropped onto the immobilized antigen and incubated for 30 min, and release of granular contents was measured. Figure 7A shows that, while changes were small, a detectable and dose-dependent increase in degranulation was apparent in RBL-Lyn^{KO} cells, a cell line for which there was no response at all with soluble DF3 (Fig 1A). In a second experiment, we reduced the potential applied force by generating a less rigid DNP-BSA. To achieve this, we conjugated BSA with DNP-PEG$_{12}$ via N-hydroxy-succinimidyl esterification (DNP-PEG$_{12}$-BSA), which places a flexible

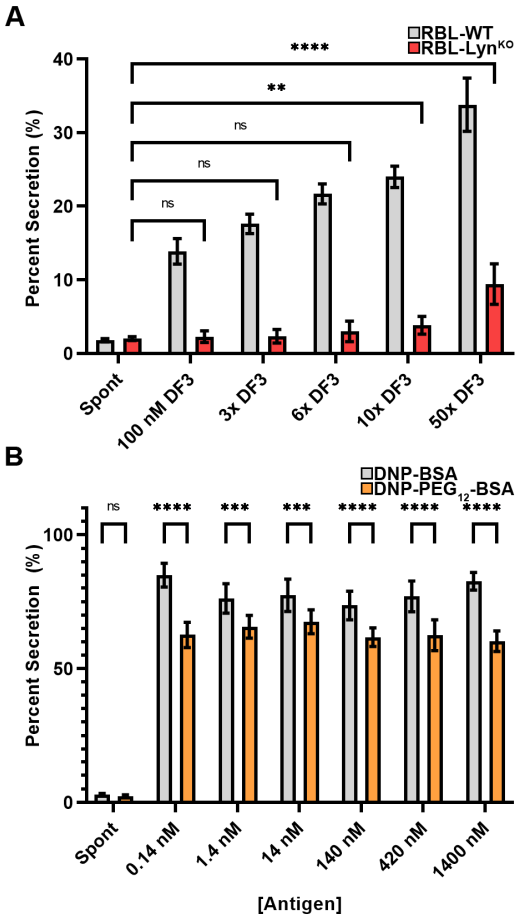

Figure 7. Alterations in antigen rigidity modulate mast cell degranulation. A) Degranulation results comparing RBL-WT and RBL-Lyn^{KO} cells in response to surface-bound DF3. Immobilized DF3 was presented at increasing concentrations on the surface of a 24-well plate and a dose dependent increase in degranulation was observed. **B)** Degranulation results from RBL-WT cells comparing activation with DNP-BSA to the less rigid DNP-PEG$_{12}$-BSA. Error bars represent SD. n=9 wells across 3 replicate experiments. ** $P < 0.01$, *** $P < 0.001$, **** $P < 0.0001$ Student's T-test over Spontaneous (A) and two-way ANOVA with Sidak's multiple comparison (B).

12-mer PEG linker between every DNP and its binding site on the BSA. The valency of DNP-PEG_{12}-BSA was found to be an average of 19, higher than the commercial DNP-BSA. Figure 7B shows that introduction of the flexible linker resulted in reduced mast cell degranulation, even with a higher average number of DNP haptens presented on the surface. These results support the notion that mechanical forces play a role in optimizing FcεRI signaling.

Discussion

FcεRI outcomes are finely tuned by an intricate combination of molecular mechanisms. In this study, we sought to better understand how the mechanisms governing FcεRI signaling are tailored in response to specific structural properties of the antigen. We began by comparing the signaling efficiency of the larger, multivalent DNP-BSA with the smaller, trivalent DF3. Degranulation assays showed that each antigen evoked a distinct response, with DNP-BSA causing robust degranulation at all doses and DF3 exhibiting high-dose inhibition (Fig. 1,2). By removing critical signaling molecules via CRISPR/Cas-9 knockout, we found that DF3-induced degranulation is highly sensitive to Lyn and SHIP1, while DNP-BSA degranulation was relatively unaffected (Fig 1,2). However, at the level of receptor phosphorylation, an influence of SHIP1 and Lyn was seen in FcεRI γ-phosphorylation patterns for both antigens (Fig. 3). While receptor phosphorylation was altered by changing the availability of signaling molecules, the robust degranulation response with DNP-BSA suggests that the geometry of this antigen initiates highly efficient signaling, easily recruiting alternative SFKs when Lyn is absent (RBL-Lyn^{KO} cells, (25)) and overcoming SHIP1 inhibition. The sensitivity of DF3 to the presence of Lyn and SHIP1 indicates that varying antigen valency and/or epitope spacing can change the ability of FcεRI to recruit proteins to the signalosome. In this case, DF3 does not efficiently phosphorylate FcεRI or initiate degranulation in the absence of Lyn (Fig. 1,3). Furthermore, we found that at high antigen doses, DF3 aggregates recruit more SHIP1 than DNP-BSA aggregates, consistent with SHIP1's effect on high dose inhibition (Fig. 2). These results demonstrate that the geometry of distinct antigens can create signaling environments that modulate the recruitment of interaction partners, both positive and negative.

The efficient recruitment of signaling molecules to the signalosome depends on several factors. Here, we have shown that the availability of phosphotyrosines for SH2-containing molecule binding is altered between the two antigens. Previous work has shown that Syk can bind to mono-phosphorylated g, given that the g subunits are in a disulfide linked dimer (25, 33). This flexibility in Syk SH2 binding modes may explain how DF3 can elicit a robust degranulation response in wild type cells even though the phosphorylation profile is incomplete (Fig 3). In RBL-SHIP1KO cells, we saw that the high dose inhibition with DF3 stimulation was abrogated. This increased degranulation corresponded with a more complete g phosphorylation profile (increase in pY4, Fig 3B) that may simply allow for increased Syk recruitment. However, we have also shown previously that altering Syk dynamics can have dramatic effects on signaling outcomes (25, 36). In fact, we showed that the presence of SHIP1 at the receptor aggregate works to reduce the Syk dwell time in the signalosome, leading to reduced Syk phosphorylation and downstream signaling (25). Therefore, the combination of receptor phosphorylation states and the interplay between recruited signaling partners work together to tune outcomes.

Another possible factor for signalosome regulation is changes in the surrounding lipid environment that drive recruitment of PH-domain-containing and palmitoylated/myristoylated proteins, such as Lyn. For example, Davey et al used FRET between IgE-AF488-FcεRI and diI-C_{18} to show that the receptor associates with cholesterol-enriched membrane domains after DNP-BSA crosslinking (59), supporting a role for ordered membrane domains in bringing Lyn to the receptor. The aggregate environment may also include or exclude signaling partners due to size or the effects of condensate formation (60, 61). Determining how antigens organize receptors in the plasma membrane is needed to understand how these distinct signaling platforms are established. Using a novel super-resolution analysis method, we were able, for the first time, to compare the nanoscale organization of individual receptors within DNP-BSA and DF3 aggregates on intact cells (Fig. 4). We found that DF3 aggregates are smaller than DNP-BSA aggregates. Measurements of circularity also suggest that DF3 aggregates are shifted towards a more linear shape. This change in shape can be interpreted as a loss in complexity due to reduced branching. We also determined the nearest neighbor spacing for receptors within aggregates and found that DF3 aggregates are more closely packed than those of DNP-BSA. The difference in receptor density may coordinate the lipid environment, as evidenced by the interplay between protein condensates and lipid organization (60). Along the same line, smaller and less complex DF3 aggregates may enable easier phosphatase access, possibly explaining the reduction in γ phosphorylation (62, 63). More work is needed to make the links between these interconnected mechanisms. Nevertheless, the super-resolution results demonstrate that differences in antigen properties are directly translated into distinct aggregate geometries, linking aggregate organization to receptor response.

Antigens may also mediate receptor responses through the induction of structural changes. Prior evidence has demonstrated that immunoreceptors undergo subunit conformational rearrangements that are correlated with activity (30–32, 53, 64–66). Initial work from Sigalov et al 2006 showed *in vitro* that CD3, Igα/β and FcεRIγ cytoplasmic domains bind to lipid vesicles as a function of positively charged headgroups. Work from multiple groups have followed-up on this observation, using live cell FRET to monitor the proximity of ITAM-containing cytoplasmic tails using a donor fluorophore on the ITAM tail and an acceptor dye (R18) intercalated into the plasma membrane (31, 53, 67, 68) These experiments showed that TCR CD3 subunit cytoplasmic tails are closer to the plasma membrane in resting cells than in activated cells. The concerted movement away from the membrane was attributed to increases in the local calcium concentration that alters the ionicity of the inner leaflet to release the ITAM from the membrane. This supports a model of ITAM activation where ITAM tails interact with the plasma membrane in resting cells, but upon ligand-induced activation ITAMs move away from the membrane to reveal the tyrosines for phosphorylation. In contrast, work on the IgM-BCR has shown the opposite behavior. Lee et al found that Igα and Igβ cytoplasmic ITAM domains do not associate with the membrane in resting cells. Upon activation, FRET was increased between Igα and the membrane, but not Igβ (65). In earlier work, Tolar et al took a different approach to monitoring receptor conformation by labeling the IgM- or IgG-BCR cytoplasmic tails directly with donor/acceptor pairs and found that the tails are spaced further apart after clustering, which was dependent on Lyn phosphorylation (32). In addition, The Reth group has shown that

conformational changes and downstream signaling are BCR isotype and antigen presentation dependent (69). While these studies in TCR and BCR have suggested a role for structural changes in regulation of ITAM function, this had not yet been explored for FcεRI. Using FRET-FLIM, we showed that the intramolecular spacing between either β-γ or γ-γ subunits is reduced upon antigen binding in living cells (Fig. 5). This is consistent with the idea that immunoreceptors undergo conformational changes in response to antigen engagement. However, our results suggest that FcεRI becomes more compact, or ordered, in structure, which is in contrast to the BCR results showing that the receptor opens up after clustering (32). Importantly, the extent of FRET observed between FcεRI subunits was positively correlated with the signaling strength of the antigen engaged. These FRET changes do not appear to be dependent on ITAM phosphorylation because there was no difference in RBL-Lyn^{KO} cells that have significantly impaired γ-pY and no detectable β-pY (25). Therefore, while subunit rearrangement appears to be a generalizable mechanism for ITAM regulation, each immunoreceptor is unique in its implementation.

Mechanotransduction is a well characterized mechanism for the regulation of BCR and TCR signaling (70–73). We, among others, have shown that monovalent ligands presented on an SLB can activate FcεRI signaling (14, 15, 63). Here, we showed that monovalent DNP-SLB can support FcεRI conformational changes, albeit to a lesser degree than soluble DNP-BSA (Fig. 6). Multiple mechanisms may influence signaling via the mast cell synapse, including application of mechanical force, increased concentration of receptors as they accumulate in the synapse and kinetic segregation of positive and negative signaling partners. Each of these mechanisms may play a role, but the fact that the observed FcεRI structural changes are Lyn-independent supports the ability of force to promote signaling. Indeed, immobilization on a surface converted non-signaling, soluble DF3 into an antigen capable of driving secretion in RBL-Lyn^{KO} cells. Conversely, introduction of a flexible PEG12 linker between each DNP hapten on DNP-BSA weakened the degranulation response (Fig. 7). These results confirm a role for mechanosensing in the tuning of FcεRI response to antigen. The force experienced by a receptor may be varied by antigen size, valency, flexibility, and presentation. Therefore, one possible explanation for the observed differences in signaling by DNP-BSA and DF3 is that the geometric constraints imposed by the antigen result in forces upon the receptor that more or less efficiently facilitate signaling.

There are over 2000 human allergens catalogued (74) but the link between the severity of the allergic response and the structural properties of the allergen requires additional inquiry. Here, we have used antigens with distinct structural properties to understand how FcεRI tunes responses to stimuli. We demonstrated that FcεRI behavior can be modified by the antigen at multiple levels, including modulation of conformational changes, ITAM phosphorylation and composition of the signalosome. The strength of FcεRI signaling was further coupled to the spatial organization of the antigen-induced aggregates as well as the ability of an antigen to impose force on the receptor. Thus, we have identified a set of mechanisms that contribute to the ability of FcεRI to overcome the threshold for activation.

Author Contributions

D.A.R., W.K.K., B.S.W., D.S.L. conceived the overall project. D.A.R was responsible for FRET-FLIM studies and most biochemical experiments described here, with assistance from H.C.K, M.P.P, R.M.G, S.L.L. W.K.K. was responsible for the dSTORM studies with assistance from D.A.R and M.J.W. on analysis. Super-resolution imaging and BAMF analysis methods were developed by K.A.L. and M.J.W. D.S.L supervised the overall project. D.S.L and D.A.R. wrote the manuscript, on which all authors commented.

Declaration of Interests

The authors have no competing interests to declare.

Acknowledgments

This work was supported by the National Institutes of Health R35GM126934 to DSL, R21GM132716 and 1R01GM140284 to KAL. MPP was supported by UNM U-RISE 1T34GM145428 01. We thank Dr. Cedric Cleyrat and Eunice Choi for generation of the knockout cell lines and initial degranulation experiments. We thank Danielle Burke for assistance with plasmid generation and Dr. Mara Steinkamp for helpful discussion. We gratefully acknowledge use of the University of New Mexico Cancer Center fluorescence microscopy and flow cytometry facilities, as well as NIH-NCI support via P30CA118100 for these cores. This work was conducted with support from the University of New Mexico Office of the Vice President for Research Program for Enhancing Research Capacity, was supported by grants from NVIDIA and utilized an NVIDIA A6000 GPU.

References

1. Lee, T.D.G., M. Swieter, and A.D. Befus. 1986. Mast cell responses to helminth infection. *Parasitology Today*. 2:186–191.
2. Lorenzo, G. Di, P. Mansueto, M. Melluso, G. Candore, A. Colombo, M.E. Pellitteri, A. Drago, M. Potestio, C. Caruso, and B. Palermo. 1997. Allergic rhinitis to grass pollen: Measurement of inflammatory mediators of mast cell and eosinophils in native nasal fluid lavage and in serum out of and during pollen season. .
3. De Weck, A.L. 1984. Pathophysiologic mechanisms of allergic and pseudo-allergic reactions to foods, food additives and drugs. *Ann Allergy*. 53.
4. Atherton, D.J. 1984. Diagnosis and management of skin disorders caused by food allergy. *Ann Allergy*. 53.
5. Galli, S.J., P. Starkl, T. Marichal, and M. Tsai. 2017. Mast Cells and IgE can Enhance Survival During Innate and Acquired Host Responses to Venoms. *Trans Am Clin Climatol Assoc*. 128.
6. Mahajan, A., D. Barua, P. Cutler, D.S. Lidke, F.A. Espinoza, C. Pehlke, R. Grattan, Y. Kawakami, C.S. Tung, A.R.M. Bradbury, W.S. Hlavacek, and B.S. Wilson. 2014. Optimal aggregation of FcεRI with a structurally defined trivalent ligand overrides negative regulation driven by phosphatases. *ACS Chem Biol*. 9.
7. Mahajan, A., L.A. Youssef, C. Cleyrat, R. Grattan, S.R. Lucero, C.P. Mattison, M.F. Erasmus, B. Jacobson, L. Tapia, W.S. Hlavacek, M. Schuyler, and B.S. Wilson. 2017. Allergen Valency, Dose, and FcεRI Occupancy Set Thresholds for Secretory Responses to Pen a 1 and Motivate Design of Hypoallergens. *The Journal of Immunology*. 198.

8. Gieras, A., B. Linhart, K.H. Roux, M. Dutta, M. Khodoun, D. Zafred, C.R. Cabauatan, C. Lupinek, M. Weber, M. Focke-Tejkl, W. Keller, F.D. Finkelman, and R. Valenta. 2016. IgE epitope proximity determines immune complex shape and effector cell activation capacity. *Journal of Allergy and Clinical Immunology*. 137.
9. Holowka, D., D. Sil, C. Torigoe, and B. Baird. 2007. Insights into immunoglobulin E receptor signaling from structurally defined ligands. *Immunol Rev*. 217:269–279.
10. Sil, D., J.B. Lee, D. Luo, D. Holowka, and B. Baird. 2007. Trivalent ligands with rigid DNA spacers reveal structural requirements for IgE receptor signaling in RBL mast cells. *ACS Chem Biol*. 2.
11. Paar, J.M., N.T. Harris, D. Holowka, and B. Baird. 2002. Bivalent Ligands with Rigid Double-Stranded DNA Spacers Reveal Structural Constraints on Signaling by FcεRI. *The Journal of Immunology*. 169.
12. Andrews, N.L., J.R. Pfeiffer, A.M. Martinez, D.M. Haaland, R.W. Davis, T. Kawakami, J.M. Oliver, B.S. Wilson, and D.S. Lidke. 2009. Small, Mobile FcεRI Receptor Aggregates Are Signaling Competent. *Immunity*. 31.
13. Spendler, K., A. Carroll-Portillo, K.A. Lidke, B.S. Wilson, J.A. Timlin, and J.L. Thomas. 2010. Distribution and dynamics of rat basophilic leukemia immunoglobulin e receptors (fcεri) on planar liqand-presentinq surfaces. *Biophys J*. 99.
14. Carroll-Portillo, A., K. Spendier, J. Pfeiffer, G. Griffiths, H. Li, K.A. Lidke, J.M. Oliver, D.S. Lidke, J.L. Thomas, B.S. Wilson, and J.A. Timlin. 2010. Formation of a Mast Cell Synapse: FcεRI Membrane Dynamics upon Binding Mobile or Immobilized Ligands on Surfaces. *The Journal of Immunology*. 184.
15. Suzuki, R., S. Leach, W. Liu, E. Ralston, J. Scheffel, W. Zhang, C.A. Lowell, and J. Rivera. 2014. Molecular editing of cellular responses by the high-affinity receptor for IgE. *Science (1979)*. 343.
16. Posner, R.G., D. Geng, S. Haymore, J. Bogert, I. Pecht, A. Licht, and P.B. Savage. 2007. Trivalent Antigens for Degranulation of Mast Cells. *Org Lett*. 9:3551–3554.
17. Gieras, A., M. Focke-Tejkl, T. Ball, P. Verdino, A. Hartl, J. Thalhamer, and R. Valenta. 2007. Molecular determinants of allergen-induced effector cell degranulation. *Journal of Allergy and Clinical Immunology*. 119:384–390.
18. Garman, S.C., B.A. Wurzburg, S.S. Tarchevskaya, J.P. Klnet, and T.S. Jardetzky. 2000. Structure of the Fc fragment of human IgE bound to its high-affinity receptor FcεRIα. *Nature*. 406.
19. Kimura, T., H. Sakamoto, E. Appella, and R.P. Siraganian. 1997. The negative signaling molecule SH2 domain-containing inositol- polyphosphate 5-phosphatase (SHIP) binds to the tyrosine-phosphorylated β subunit of the high affinity IgE receptor. *Journal of Biological Chemistry*. 272.
20. Bruhns, P., F. Vély, O. Malbec, W.H. Fridman, E. Vivier, and M. Daëron. 2000. Molecular basis of the recruitment of the SH2 domain-containing inositol 5-phosphatases SHIP1 and SHIP2 by FcγRIIB. *Journal of Biological Chemistry*. 275.
21. Hořejší, V., W. Zhang, and B. Schraven. 2004. Transmembrane adaptor proteins: organizers of immunoreceptor signalling. *Nat Rev Immunol*. 4:603–616.
22. Ivashkiv, L.B. 2009. Cross-regulation of signaling by ITAM-associated receptors. *Nat Immunol*. 10.
23. Huber, M., C.D. Helgason, J.E. Damen, L. Liu, R.K. Humphries, and G. Krystal. 1998. The src homology 2-containing inositol phosphatase (SHIP) is the gatekeeper of mast cell degranulation. *Proc Natl Acad Sci U S A*. 95.
24. Furumoto, Y., S. Nunomura, T. Terada, J. Rivera, and C. Ra. 2004. The FcεRIβ Immunoreceptor Tyrosine-based Activation Motif Exerts Inhibitory Control on MAPK and IκB Kinase Phosphorylation and Mast Cell Cytokine Production. *Journal of Biological Chemistry*. 279:49177–49187.

25. Kanagy, W.K., C. Cleyrat, M. Fazel, S.R. Lucero, M.P. Bruchez, K.A. Lidke, B.S. Wilson, and D.S. Lidke. 2022. Docking of Syk to FcεRI is enhanced by Lyn but limited in duration by SHIP1. *Mol Biol Cell*. 33.
26. Wakefield, D.L., D. Holowka, and B. Baird. 2017. The Fcεri signaling cascade and integrin trafficking converge at patterned ligand surfaces. *Mol Biol Cell*. 28.
27. Saitoh, S., R. Arudchandran, T.S. Manetz, W. Zhang, C.L. Sommers, P.E. Love, J. Rivera, and L.E. Samelson. 2000. LAT Is Essential for FcεRI-Mediated Mast Cell Activation. *Immunity*. 12:525–535.
28. Liu, F.T., J.W. Bohn, E.L. Ferry, H. Yamamoto, C.A. Molinaro, L.A. Sherman, N.R. Klinman, and D.H. Katz. 1980. Monoclonal dinitrophenyl-specific murine IgE antibody: preparation, isolation, and characterization. *The Journal of Immunology*. 124.
29. Fazel, M., M.J. Wester, D.J. Schodt, S.R. Cruz, S. Strauss, F. Schueder, T. Schlichthaerle, J.M. Gillette, D.S. Lidke, B. Rieger, R. Jungmann, and K.A. Lidke. 2022. High-precision estimation of emitter positions using Bayesian grouping of localizations. *Nat Commun*. 13.
30. Shen, Z., S. Liu, X. Li, Z. Wan, Y. Mao, C. Chen, and W. Liu. 2019. Conformational change within the extracellular domain of B cell receptor in B cell activation upon antigen binding. *Elife*. 8.
31. Gagnon, E., D.A. Schubert, S. Gordo, H.H. Chu, and K.W. Wucherpfennig. 2012. Local changes in lipid environment of TCR microclusters regulate membrane binding by the CD3ε cytoplasmic domain. *Journal of Experimental Medicine*. 209.
32. Tolar, P., H.W. Sohn, and S.K. Pierce. 2005. The initiation of antigen-induced B cell antigen receptor signaling viewed in living cells by fluorescence resonance energy transfer. *Nat Immunol*. 6.
33. Travers, T., W.K. Kanagy, R.A. Mansbach, E. Jhamba, C. Cleyrat, B. Goldstein, D.S. Lidke, B.S. Wilson, and S. Gnanakaran. 2019. Combinatorial diversity of Syk recruitment driven by its multivalent engagement with FcεRIγ. *Mol Biol Cell*. 30.
34. Metzger, H., G. Alcaraz, R. Hohman, J.P. Kinet, V. Pribluda, and R. Quarto. 1986. The receptor with high affinity for immunoglobulin E. *Annu Rev Immunol*. 4.
35. Wilson, B.S., J.R. Pfeiffer, and J.M. Oliver. 2000. Observing FcεRI signaling from the inside of the mast cell membrane. *Journal of Cell Biology*. 149.
36. Schwartz, S.L., C. Cleyrat, M.J. Olah, P.K. Relich, G.K. Phillips, W.S. Hlavacek, K.A. Lidke, B.S. Wilson, and D.S. Lidke. 2017. Differential mast cell outcomes are sensitive to fcεri-syk binding kinetics. *Mol Biol Cell*. 28.
37. Schwartz, S.L., Q. Yan, C.A. Telmer, K.A. Lidke, M.P. Bruchez, and D.S. Lidke. 2015. Fluorogen-activating proteins provide tunable labeling densities for tracking FcεRI independent of IgE. *ACS Chem Biol*. 10.
38. Schodt, D.J., F. Farzam, S. Liu, and K.A. Lidke. 2023. Automated multi-target super-resolution microscopy with trust regions. *Biomed Opt Express*. 14:429.
39. Smith, C.S., N. Joseph, B. Rieger, and K.A. Lidke. 2010. Fast, single-molecule localization that achieves theoretically minimum uncertainty. *Nat Methods*. 7:373–375.
40. Huang, X. 2011. Quasi-maximum likelihood estimation of discretely observed diffusions. *Econom J*. 14:241–256.
41. Schodt, D.J., and K.A. Lidke. 2021. Spatiotemporal Clustering of Repeated Super-Resolution Localizations via Linear Assignment Problem. *Frontiers in Bioinformatics*. 1.
42. Wester, M.J., D.J. Schodt, H. Mazloom-Farsibaf, M. Fazel, S. Pallikkuth, and K.A. Lidke. 2021. Robust, fiducial-free drift correction for super-resolution imaging. *Sci Rep*. 11:23672.
43. Sander, J., M. Ester, H.P. Kriegel, and X. Xu. 1998. Density-based clustering in spatial databases: The algorithm GDBSCAN and its applications. *Data Min Knowl Discov*. 2.

44. Daszykowski, M., B. Walczak, and D.L. Massart. 2002. On the optimal partitioning of data with K-means, growing K-means, neural gas, and growing neural gas. *J Chem Inf Comput Sci*. 42.
45. Fazel, M., M.J. Wester, H. Mazloom-Farsibaf, M.B.M. Meddens, A.S. Eklund, T. Schlichthaerle, F. Schueder, R. Jungmann, and K.A. Lidke. 2019. Bayesian Multiple Emitter Fitting using Reversible Jump Markov Chain Monte Carlo. *Sci Rep*. 9:13791.
46. Pfeiffer, J.R., J.C. Seagrave, B.H. Davis, G.G. Deanin, and J.M. Oliver. 1985. Membrane and cytoskeletal changes associated with IgE-mediated serotonin release from rat basophilic leukemia cells. *Journal of Cell Biology*. 101.
47. Rofolovitch, M., M. Amira, and H. Ginsburg. 1987. Degranulation of in vitro differentiated mast cells stimulated by two monoclonal IgE specificities. *Eur J Immunol*. 17.
48. Holowka, D., N. Calloway, R. Cohen, D. Gadi, J. Lee, N.L. Smith, and B. Baird. 2012. Roles for Ca2+ mobilization and its regulation in mast cell functions. *Front Immunol*. 3.
49. Yamashita, T., R. Suzuki, P.S. Backlund, Y. Yamashita, A.L. Yergey, and J. Rivera. 2008. Differential dephosphorylation of the FcRγ immunoreceptor tyrosine-based activation motif tyrosines with dissimilar potential for activating syk. *Journal of Biological Chemistry*. 283.
50. Jensen, L.G., T.Y. Hoh, D.J. Williamson, J. Griffié, D. Sage, P. Rubin-Delanchy, and D.M. Owen. 2022. Correction of multiple-blinking artifacts in photoactivated localization microscopy. *Nat Methods*. 19.
51. Rossboth, B., A.M. Arnold, H. Ta, R. Platzer, F. Kellner, J.B. Huppa, M. Brameshuber, F. Baumgart, and G.J. Schütz. 2018. TCRs are randomly distributed on the plasma membrane of resting antigen-experienced T cells. *Nat Immunol*. 19:821–827.
52. Van De Linde, S., A. Löschberger, T. Klein, M. Heidbreder, S. Wolter, M. Heilemann, and M. Sauer. 2011. Direct stochastic optical reconstruction microscopy with standard fluorescent probes. *Nat Protoc*. 6.
53. Shi, X., Y. Bi, W. Yang, X. Guo, Y. Jiang, C. Wan, L. Li, Y. Bai, J. Guo, Y. Wang, X. Chen, B. Wu, H. Sun, W. Liu, J. Wang, and C. Xu. 2013. Ca 2+ regulates T-cell receptor activation by modulating the charge property of lipids. *Nature*. 493.
54. Valley, C.C., K.A. Lidke, and D.S. Lidke. 2014. The spatiotemporal organization of ErbB receptors: Insights from microscopy. *Cold Spring Harb Perspect Biol*. 6.
55. Spatola Rossi, T., C. Pain, S.W. Botchway, and V. Kriechbaumer. 2022. FRET-FLIM to Determine Protein Interactions and Membrane Topology of Enzyme Complexes. *Curr Protoc*. 2.
56. Wallrabe, H., and A. Periasamy. 2005. Imaging protein molecules using FRET and FLIM microscopy. *Curr Opin Biotechnol*. 16.
57. Ghukasyan, V. 2010. Fluorescence lifetime dynamics of enhanced green fluorescent protein in protein aggregates with expanded polyglutamine. *J Biomed Opt*. 15.
58. Shaner, N.C., G.G. Lambert, A. Chammas, Y. Ni, P.J. Cranfill, M.A. Baird, B.R. Sell, J.R. Allen, R.N. Day, M. Israelsson, M.W. Davidson, and J. Wang. 2013. A bright monomeric green fluorescent protein derived from Branchiostoma lanceolatum. *Nat Methods*. 10.
59. Davey, A.M., K.M. Krise, E.D. Sheets, and A.A. Heikal. 2008. Molecular perspective of antigen-mediated mast cell signaling. *Journal of Biological Chemistry*. 283.
60. Wang, H.Y., S.H. Chan, S. Dey, I. Castello-Serrano, M.K. Rosen, J.A. Ditlev, K.R. Levental, and I. Levental. 2023. Coupling of protein condensates to ordered lipid domains determines functional membrane organization. *Sci Adv*. 9.
61. Jaqaman, K., and J.A. Ditlev. 2021. Biomolecular condensates in membrane receptor signaling. *Curr Opin Cell Biol*. 69.
62. Young, R.M., X. Zheng, D. Holowka, and B. Baird. 2005. Reconstitution of regulated phosphorylation of FcεRI by a lipid raft-excluded protein-tyrosine phosphatase. *Journal of Biological Chemistry*. 280.

63. Felce, J.H., E. Sezgin, M. Wane, H. Brouwer, M.L. Dustin, C. Eggeling, and S.J. Davis. 2018. CD45 exclusion– and cross-linking–based receptor signaling together broaden FcεRI reactivity. *Sci Signal*. 11.
64. Chen, X., W. Pan, Y. Sui, H. Li, X. Shi, X. Guo, H. Qi, C. Xu, and W. Liu. 2015. Acidic phospholipids govern the enhanced activation of IgG-B cell receptor. *Nat Commun*. 6:8552.
65. Lee, W.Y., and P. Tolar. 2013. Activation of the B cell receptor leads to increased membrane proximity of the Igα cytoplasmic domain. *PLoS One*. 8.
66. Sigalov, A.B., D.A. Aivazian, V.N. Uversky, and L.J. Stern. 2006. Lipid-binding activity of intrinsically unstructured cytoplasmic domains of multichain immune recognition receptor signaling subunits. *Biochemistry*. 45.
67. Xu, C., E. Gagnon, M.E. Call, J.R. Schnell, C.D. Schwieters, C. V. Carman, J.J. Chou, and K.W. Wucherpfennig. 2008. Regulation of T Cell Receptor Activation by Dynamic Membrane Binding of the CD3ε Cytoplasmic Tyrosine-Based Motif. *Cell*. 135.
68. Gagnon, E., A. Connolly, J. Dobbins, and K.W. Wucherpfennig. 2017. Studying dynamic plasma membrane binding of TCR-CD3 chains during immunological synapse formation using donor-quenching FRET and FLIM-FRET. In: Methods in Molecular Biology. .
69. Volkmann, C., N. Brings, M. Becker, E. Hobeika, J. Yang, and M. Reth. 2016. Molecular requirements of the B-cell antigen receptor for sensing monovalent antigens. *EMBO J*. 35:2371–2381.
70. Feng, Y., E.L. Reinherz, and M.J. Lang. 2018. αβ T Cell Receptor Mechanosensing Forces out Serial Engagement. *Trends Immunol*. 39.
71. Liu, B., W. Chen, B.D. Evavold, and C. Zhu. 2014. Accumulation of dynamic catch bonds between TCR and agonist peptide-MHC triggers T cell signaling. *Cell*. 157.
72. Natkanski, E., W.Y. Lee, B. Mistry, A. Casal, J.E. Molloy, and P. Tolar. 2013. B cells use mechanical energy to discriminate antigen affinities. *Science (1979)*. 340.
73. Wan, Z., X. Chen, H. Chen, Q. Ji, Y. Chen, J. Wang, Y. Cao, F. Wang, J. Lou, Z. Tang, and W. Liu. 2015. The activation of IgM- or isotype-switched IgG- and IgE-BCR exhibits distinct mechanical force sensitivity and threshold. *Elife*. 4.
74. Schein, C.H., S.S. Negi, and W. Braun. 2022. Still SDAPing Along: 20 Years of the Structural Database of Allergenic Proteins. *Frontiers in Allergy*. 3.